Geophysical Journal International

Geophys. J. Int. (2014) **196,** 681–693
Advance Access publication 2013 December 13

doi: 10.1093/gji/ggt464

Lithospheric 3-D flexure modelling of the oceanic plate seaward of the trench using variable elastic thickness

Paula Manríquez,[1] Eduardo Contreras-Reyes[1] and Axel Osses[2]

[1]*Departamento de Geofísica, Facultad de Ciencias Físicas y Matemáticas, Universidad de Chile, Santiago, Chile. E-mail: pmanriqu@yahoo.com*
[2]*Departamento de Ingeniería Matemática, Facultad de Ciencias Físicas y Matemáticas, Universidad de Chile and Centro de Modelamiento Matemático, UMR* 2071 *CNRS-Uchile, Santiago, Chile*

Accepted 2013 November 12. Received 2013 October 24; in original form 2012 November 26

SUMMARY

When describing the mechanical behaviour of the lithosphere modelled as a thin plate, the most important parameter corresponds to its flexural rigidity, which is commonly expressed through the effective elastic thickness, T_e. This parameter is a measure of the stiffness of the plate and defines the maximum magnitude and wavelength of those surface loads that can be supported without suffering unelastic deformation. Realistic 3-D models of the flexural response of the lithosphere near the trench are scarce because of the mathematical and computational complexity. We present a method for determining the flexure of the lithosphere caused by the combined effect of 3-D seamount loading and bending of the lithosphere near the trench. Our method consists on solving numerically the flexure equations of the Reissner–Mindlin thin plate theory, including variable thickness, using the finite element method with mesh adaptation. The method was applied to study the flexure of the oceanic Nazca lithosphere beneath the O'Higgins seamount group which lies ∼70 km seaward of the Chile trench. The results show that an elastic thickness T_e of ∼5 km under the seamounts, a T_e of ∼15 km far from the trench and a T_e of ∼13 km near the trench can explain both, the down deflection of the oceanic Moho and bending of the oceanic lithosphere observed in seismic and gravity profiles. In order to study the impact of high trench curvature on the morphology of the outer rise, we apply the same methodology to study and model the flexure of the lithosphere in the Arica Bend region (14°S–23°S). Results indicate that the T_e values are overestimated if the 3-D trench curvature is not included in the modelling.

Key words: Numerical approximations and analysis; Dynamics of lithosphere and mantle; Lithospheric flexure; Folds and folding; Mechanics, theory and modelling.

1 INTRODUCTION

Plate tectonics is based on the assumption that the lithosphere behaves as a thin competent (elastic, plastic) plate overlying an inviscid fluid (asthenosphere) that flexes in response to applied stresses at geological time (i.e. $>10^6$ yr) and space scales. The main evidence for its rigid behaviour comes from studies of the way that it responds to surface loads such as ice-sheets, sediments and volcanoes (e.g. Watts 2001). In the description of its mechanical behaviour, the parameter that characterizes the stiffness or resistance of the lithosphere to deformation is the flexural rigidity D, which is commonly expressed in terms of the elastic thickness (T_e) of the lithosphere. T_e is therefore a proxy of its strength and could be understood as the thickness of an equivalent elastic plate overlying and inviscid fluid that would bend in the same way that the real lithosphere would. The plate strength is controlled at least by three equally important physical properties, such as plate age and thermal state, composition and inelastic deformation among others. These are discussed in detail in Section 4.

The shape of the flexure of the lithosphere has been modelled by many authors in order to determine some of its mechanical properties (Walcott 1970; Watts *et al.* 1975; Bodine & Watts 1979; Judge & McNutt 1991; Wessel 1996; Braitenberg *et al.* 2002).

In this work, we study the flexure of the oceanic lithosphere caused by the combined effect of seamount loading and bending of the lithosphere near the trench. Currently, realistic 3-D models are scarce because they are not able to model the flexure caused by the combined effect of the subduction of a plate with the one that is produced by a given load (e.g. seamount). This is mainly due to the large computational consumption and the associated mathematical complexity. An interesting model is the one proposed by Hertz (1884) and which was later used in the work of Walcott (1970) and Watts *et al.* (1975) among others. The model proposed by Hertz (1884) corresponds to an analytical solution of the flexure equation, which

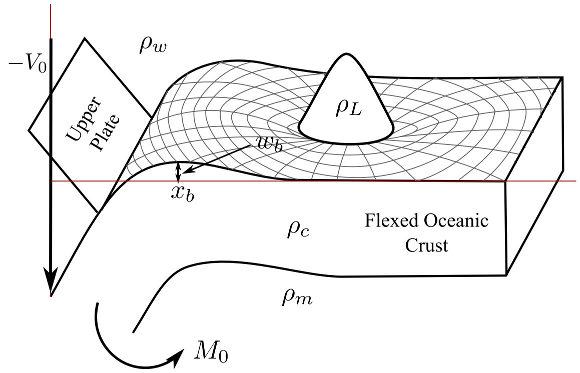

Figure 1. Cartoon of the flexure produced by the combined effect of seamount loading and subduction in the trench. ρ_w is the water density, ρ_L the applied load (seamount) density, ρ_c the crust's density and ρ_m is the mantle's density. M_0 is the bending moment and V_0 is the vertical shear force.

allows to calculate the deflection produced by a 3-D load away from a subduction zone. However, the results in terms of amplitude of the deflection are not as expected since the calculated amplitudes of displacement are less than half those observed, although the calculated flexure wavelengths are consistent with observations (Walcott 1970).

On the other hand, there are models that can combine the effects of plate subduction at the trench with the effects caused by the existence of a topographic load (Fig. 1). However, these models have important limitations as they consider a load that is infinite in one direction, that is a 2-D loading which could be appropriate to linear geological features such as seamount chains and aseismic ridges. Furthermore, they consider that the plate subducts perpendicular to the trench with a constant azimuth (Hanks 1971; Watts & Talwani 1974; Parsons & Molnar 1976; Harris & Chapman 1994; Levitt & Sandwell 1995; Bry & White 2007) which is an unrealistic approximation for margins where the trench axis has a strong curvature.

In this paper we study two areas. The first one corresponds to the Nazca oceanic plate beneath the Juan Fernandez ridge located about 70 km west of the Chilean coast at the same latitude of Valparaíso as shown in Fig. 2. In this area, we study the deflection caused by two seamounts: the O'Higgins Guyot and the O'Higgins Seamount, including the deformation caused by the subduction of the Nazca Plate beneath the South American continental plate. This will allow the determination of the distribution of elastic thickness of the lithosphere, which we assume variable. For the flexural modelling, we use gravity data constraining the geometry of the oceanic Moho. The second study zone is the area known as the Arica Bend, located in north Chile. The particularities of this area are that the convergence direction is not perpendicular to the trench and the strong curvature of the trench axis.

We propose a plate deflection forward model that numerically solves the fundamental flexure equations of the Reissner–Mindlin (R–M) thin plate theory using the finite element method (FEM) with variable elastic thickness.

2 FORMULATION AND IMPLEMENTATION OF THE METHOD

2.1 The R–M plate model

The R–M model considers a thin elastic plate which elastic thickness is given by $T_e(x, y)$ and that there are external forces acting

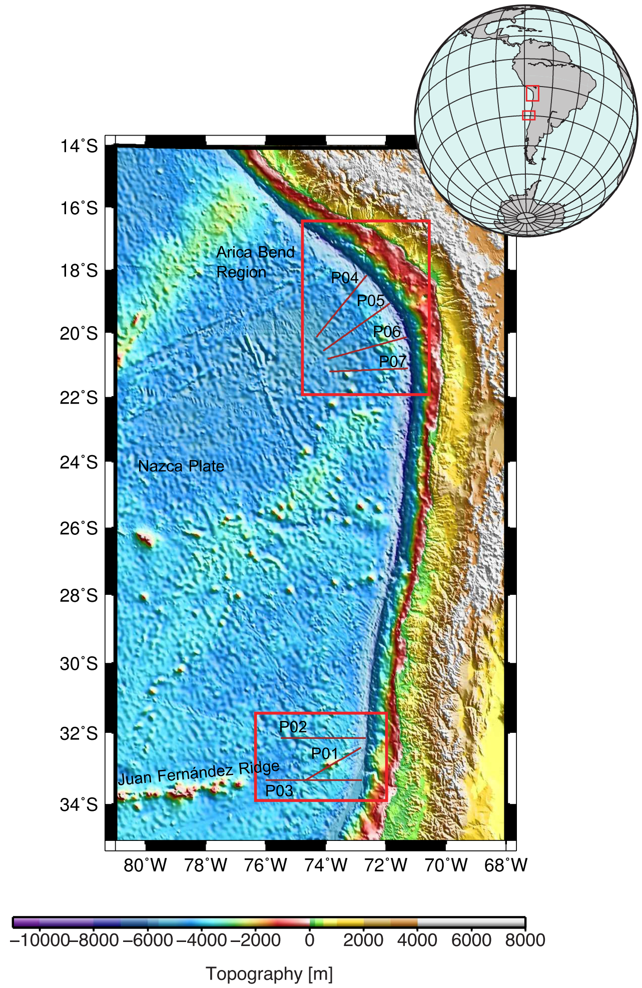

Figure 2. Bathymetry for both study zones obtained from global free data sets available at http://topex.ucsd.edu/. The southern zone in the red box corresponds to our first study area and is part of the Juan Fernández Ridge. The northern zone in the red box is known as the Arica Bend region. In red the studied profiles for both regions.

perpendicular to its middle surface (Mindlin 1951). The plate is defined as $\Omega \times [-\frac{T_e(x,y)}{2}, \frac{T_e(x,y)}{2}]$, with $\Omega \in \mathbb{R}^2$. Its lateral border is given by $\partial\Omega \times [-\frac{T_e(x,y)}{2}, \frac{T_e(x,y)}{2}]$.

Let $\vec{u}$ be the displacement vector. The hypotheses of the R–M plate theory are (Braess 2007):

H1. *Linearity hypothesis*. Segments lying on normals to the mid-surface are linearly deformed and their images are segments on straight lines again.

H2. The displacement in the z-direction does not depend on the z-coordinate: $u_3(x, y, z) = w(x, y)$.

H3. The points on the mid-surface are deformed only in the z-direction: $u_1(x, y, 0) = u_2(x, y, 0) = 0$.

H4. The normal stress σ_{33} vanishes.

The fundamental equations are given by Reissner (1945) and Mindlin (1951)

$$-\mathrm{div}[T_e^3\sigma(\vec{\theta})] - \lambda^* T_e(\nabla w - \vec{\theta}) = 0 \quad (1)$$

$$-\mathrm{div}[\lambda^* T_e(\nabla w - \vec{\theta})] = g, \quad (2)$$

where $\lambda^* = k \cdot \mu$, with $k = \frac{5}{6-\nu}$. The parameter k is known as the Timoshenko shear coefficient, which is an adjustment parameter in thick plate, beam and shell equations of motion that is included to compensate for stress distribution in the cross-sectional shape of the object (Hull 2004). The parameter μ is one of the Lamé coefficients and ν is the Poisson's ratio.

The total vertical force that experiments the plate is given by g, and corresponds, in our problem, to the vertical forces acting downwards due to bathymetric loading $q(x, y)$, for example a seamount, and an hydrostatic restoring force acting upwards proportional to the vertical displacement of the plate w and the density difference between the overlying water and the underlying mantle rock $\Delta\rho = \rho_{\mathrm{m}} - \rho_{\mathrm{w}}$. Then

$$g(x, y) = q(x, y) - (\rho_{\mathrm{m}} - \rho_{\mathrm{w}})gw = q(x, y) - \Delta\rho\, g\, w. \tag{3}$$

We call w the transverse displacement or (normal) deflection, and $\vec{\theta} = (\theta_1, \theta_2)$ the rotation. $\sigma(\vec{\theta})$ is the stress tensor defined as

$$\sigma(\vec{\theta}) = \bar{D}\left[(1-\nu)\varepsilon(\vec{\theta}) + \nu \mathrm{tr}(\varepsilon(\vec{\theta}))I_{2\times 2}\right],$$

where $\bar{D} = \frac{E}{12(1-\nu)}$, E is the Young's modulus and $\varepsilon(\vec{\theta})$ corresponds to the 'strain tensor'

$$\varepsilon(\vec{\theta}) = \frac{1}{2}\left[\nabla\vec{\theta} + (\nabla\vec{\theta})^T\right] \quad \text{or} \quad \varepsilon_{ij}(\theta) = \frac{1}{2}\left(\frac{\partial\theta_i}{\partial x_j} + \frac{\partial\theta_j}{\partial x_i}\right).$$

In a more explicit form

$$\sigma(\vec{\theta}) =$$

$$\bar{D}\begin{bmatrix} (1-\nu)\partial_x\theta_1 + \nu(\partial_x\theta_1 + \partial_y\theta_2) & \frac{(1-\nu)}{2}(\partial_y\theta_1 + \partial_x\theta_2) \\ \frac{(1-\nu)}{2}(\partial_y\theta_1 + \partial_x\theta_2) & (1-\nu)\partial_y\theta_2 + \nu(\partial_x\theta_1 + \partial_y\theta_2) \end{bmatrix}.$$

We also introduce the flexural rigidity defined as

$$D(x, y) := T_{\mathrm{e}}^3(x, y) \cdot \bar{D}(x, y).$$

If a fifth hypothesis, known as the 'normal hypothesis' or 'Kirchhoff's hypothesis', is added the Kirchhoff–Love equation of motion for an elastic plate can be derived (see the Appendix).

2.2 Finite element method

The FEM was used for numerically solve the problem given in eqs (1) and (2) using the FreeFem++ software.

The FEM is one of the most powerful and used methods for numerically solving boundary and initial value problems characterized by partial differential equations and it has had great impact on engineering and science. The development of the essence of the method is attributed mainly to the German mathematician Richard Courant (1888–1972).

2.3 Domain and boundary conditions

Prior to the variational formulation construction, the boundary conditions of the problem must be fixed. For a rectangular domain, let Γ_1 be the subducting border, Γ_2 one of the lateral free borders, Γ_3 a fixed border that represents the plate far away from the trench where there no flexure occurs (hard clamped) and Γ_4 the other lateral free border (for example, see Fig. 3c).

At the boundary, if $\hat{n}$ denotes the exterior unit normal vector, the shear force and bending moment are, respectively, given by

$$V = \lambda^* T_{\mathrm{e}}\left(\frac{\partial w}{\partial n} - \vec{\theta}\cdot\hat{n}\right) \quad \text{and} \quad \vec{M} = T_{\mathrm{e}}^3\sigma(\vec{\theta})\hat{n} \tag{4}$$

which in both cases, act with a fixed value over the subducting edge Γ_1. These values, M_0 and V_0 were determined using the 1-D approximation shown in Turcotte & Schubert (2002).

$$M_0 = \frac{2A\cdot D_0}{\alpha^2}\cdot \mathrm{e}^{x_0/\alpha}\cdot\cos\left(\frac{x_0}{\alpha}\right)$$

$$V_0 = -\frac{2A\cdot D_0}{\alpha^3}\cdot M^{x_0/\alpha}\cdot\left[\cos\left(\frac{x_0}{\alpha}\right) - \sin\left(\frac{x_0}{\alpha}\right)\right],$$

where (see Fig. 1) $D_0 = \frac{E\cdot T_{e_1}^3}{12\cdot(1-\nu^2)}$, $\alpha = [\frac{4\cdot D_0}{(\rho_{\mathrm{m}}-\rho_{\mathrm{w}})g}]^{1/4}$, $x_0 = x_b - \alpha\cdot\frac{\pi}{4}$ and $A = w_{\mathrm{b}}\sqrt{2}\cdot\mathrm{e}^{\pi/4}$.

The boundary conditions for a rectangular domain are given by

$$\begin{aligned} &\Gamma_1: && \vec{M} = -\vec{M}_0 = -M_0\hat{\beta}, \quad V = -V_0 \\ &\Gamma_2: && \vec{M} = 0, \quad V = 0 \\ &\Gamma_3: && w = 0, \quad \vec{\theta} = 0 \\ &\Gamma_4: && \vec{M} = 0, \quad V = 0, \end{aligned}$$

where $\hat{\beta}$ corresponds to the unitary vector in the plate convergence direction (Fig. 4b).

The total vertical force that experiments the plate $g(x, y)$ corresponds to the sum of the load due to the bathymetry $q(x, y)$ (for example, a seamount as the O'Higgins Guyot) minus an hydrostatic restoring force in the opposite direction following eq. (3).

The constants used for the numerical modelling are shown in Table 1.

2.4 Variational formulation for the R–M plate model

The variational formulation of the problem in eqs (1) and (2) is given by (see the Appendix for more detail).

$$\begin{aligned} &\text{Find } (\vec{\theta}, w, \vec{\gamma}, d) \text{ such that } \int_\Omega T_{\mathrm{e}}^3\bar{D}(1-\nu)\varepsilon(\vec{\theta}):\varepsilon(\vec{\psi}) \\ &+ \int_\Omega T_{\mathrm{e}}^3\bar{D}\nu\mathrm{div}(\vec{\theta})\mathrm{div}(\vec{\psi}) + \int_\Omega \vec{\gamma}\cdot(\nabla v - \vec{\psi}) \\ &+ \int_\Omega T_{\mathrm{e}}\lambda^*(\nabla w - \vec{\theta})\cdot\vec{\eta} - \int_\Omega \vec{\gamma}\cdot\vec{\eta} + \int_\Omega T_{\mathrm{e}}^3\bar{D}\nu\mathrm{div}(\vec{\theta})e \\ &- \int_\Omega T_{\mathrm{e}}^3\bar{D}\nu\, d\, e + \int_\Omega \Delta\rho g\, w\, v \\ &= \int_\Omega q v - \int_{\Gamma_1} V_0 v - \int_{\Gamma_1} M_0\hat{\beta}\cdot\vec{\psi} \quad \text{for all } (\vec{\psi}, v, \vec{\eta}, e), \end{aligned} \tag{5}$$

where $(\vec{\theta}, w)$ and $(\vec{\psi}, v)$ (test functions for $\vec{\theta}$ and w, respectively) are prescribed to be zero on the same boundaries, as indicated in Section 2.3. Note that the term $\hat{\beta}\cdot\vec{\psi}$ should be written in an intrinsic reference system to the boundary. If $\hat{\beta} = (\cos\beta, \sin\beta)$, $\hat{n} = (n_x, n_y)$ and $\hat{\tau} = (-n_y, n_x)$ (Fig. 4b), then

$$\hat{\beta}\cdot\vec{\psi} = \begin{bmatrix} (n_x\cos\beta + n_y\sin\beta)(n_x\psi_1 + n_y\psi_2) \\ (n_x\sin\beta - n_y\cos\beta)(n_x\psi_2 - n_y\psi_1) \end{bmatrix}, \tag{6}$$

where β is the subduction angle with respect to the horizontal reference.

The previous formulation (5) of the original problem (1)–(2) was programmed in the variational framework of the FreeFem++ software. In order to approximate w, v, $\vec{\theta} = (\theta_1, \theta_2)$ and $\vec{\psi} = (\psi_1, \psi_2)$ triangular finite elements of type 'P2' were used. To approximate $\vec{\gamma} = (\gamma_1, \gamma_2)$, $\vec{\eta} = (\eta_1, \eta_2)$, d and e we used triangular finite elements of type P1.

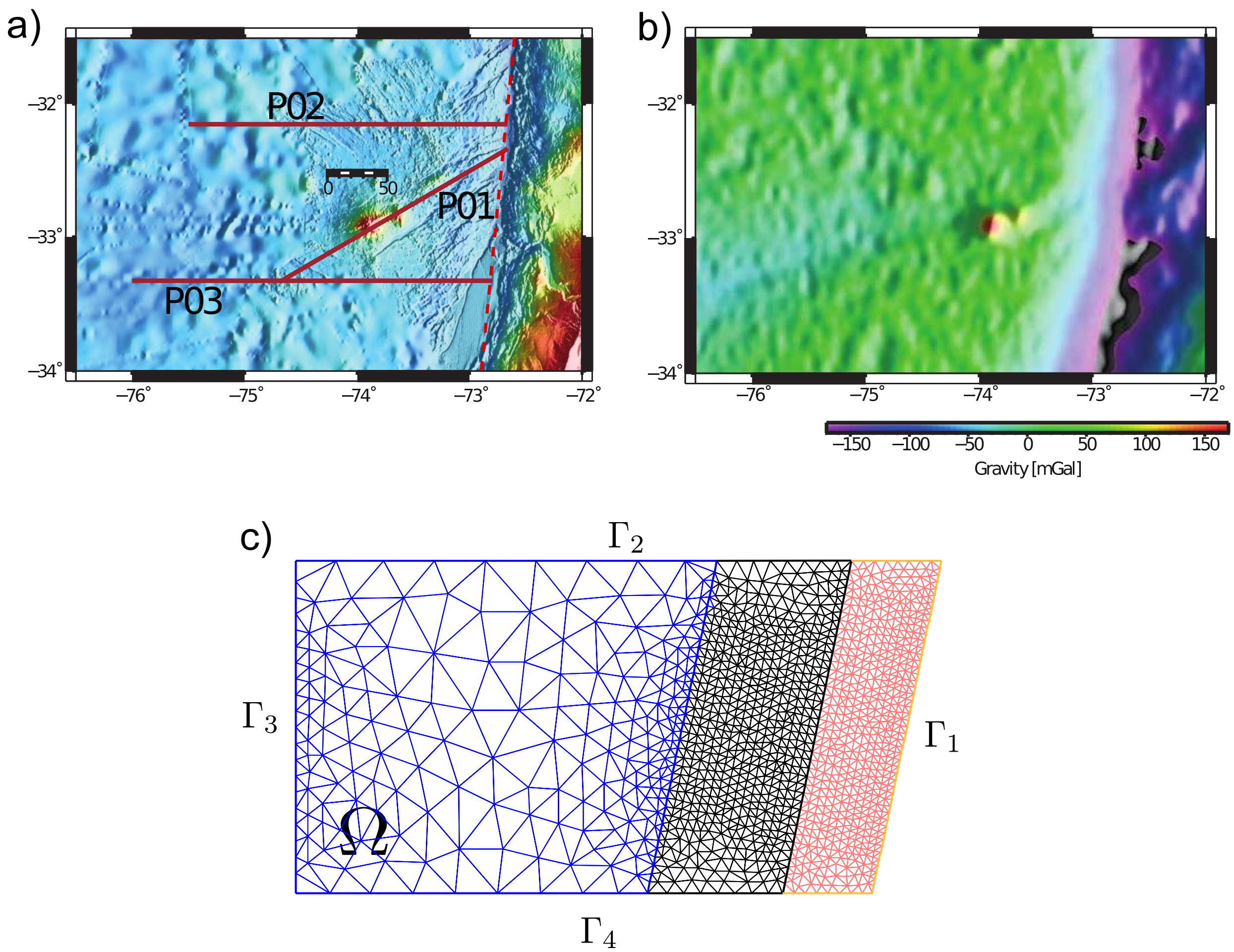

Figure 3. (a) High resolution bathymetry of the first study area and the three studied profiles: P01, P02 and P03 in red. (b) Gravity anomaly plot expressed in (mGal) (Sandwell & Smith 1997). (c) Starting mesh used for flexure calculation through FEM for the Juan Fernández region. The domain was divided into three areas in which the elastic thickness was varied. The area closest to the trench (S1) ranges from 0 to 60 km away from the trench (pink), the second area (S2) from 60 to 150 km (black) and the third (S3) from 150 km to the end of the plate (blue).

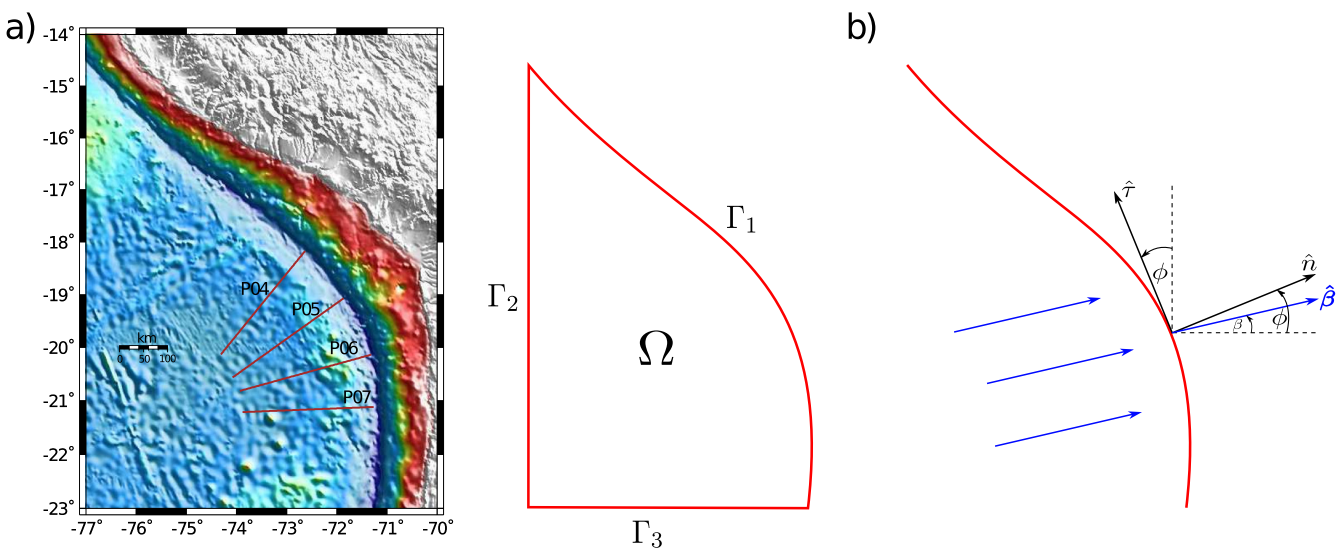

Figure 4. (a) Second domain used for the flexure calculation through FEM for the Arica Bend region. (b) Border Γ_1 for the domain used for the second studied zone, the Arica Bend, shown in red line. The convergence direction is shown in blue, $\hat{n}$ and $\hat{\tau}$ correspond to the normal and the tangent to the plate border respectively and ϕ corresponds to the angle formed by the normal to the plate border and the horizontal.

Table 1. Values of parameters and constants used in flexural modelling.

Name	Symbol	Value	Unit
Young's modulus	E	70×10^9	Pa
Acceleration due to gravity	g	9.8	$\mathrm{m\,s^{-2}}$
Poisson's ratio	ν	0.25	
Mantle density	ρ_m	3300	$\mathrm{kg\,m^{-3}}$
Crust density	ρ_c	2700	$\mathrm{kg\,m^{-3}}$
Sediment density	ρ_s	2000	$\mathrm{kg\,m^{-3}}$
Water density	ρ_w	1030	$\mathrm{kg\,m^{-3}}$

3 APPLICATION OF THE METHOD

3.1 Comparison with other approaches

To validate our R–M formulation, we calculated the flexure produced by some simple loads and compared our results with those given by already-established and well-tested methods under identical configurations of loads, elastic thickness structure and boundary conditions.

First we calculated the flexure produced by a rectangular load of 5 km high, 40 km wide and 400 km long (1-D load). The mesh used was a rectangular mesh of 500 km long and 400 km wide. The elastic thickness was varied along the plate and thus the mesh was divided into three distinct regions. The first ranges from 0 to 100 km away from the trench ($T_e = 10$ km), the second from 100 to 200 km away from the trench ($T_e = 15$ km) and the third from 200 to 500 km ($T_e = 20$ km). In Fig. 5(a), we show the elastic thickness variation in green (right-hand axis) and the load used in blue dotted line (left-hand axis). Both curves are expressed in kilometres. At the bottom of the figure (Fig. 5b) in light blue the result of the 1-D Kirchhoff–Love model solved using a variable elastic thickness through the finite difference method shown in the work of Contreras-Reyes & Osses (2010). In purple dotted line, the result of the 2-D R–M model using $\beta = 0^{\circ}$. It can be seen that the fit is very good and there are only minor differences in the part of the bulge ~50 km away from the trench.

Then, we calculated the flexure produced by a rectangular load with a square base of 100 km long, 100 km wide and 5 km high located at the centre of an elastic plate of constant elastic thickness ($T_e = 15$ km) of 1200 km × 1200 km. It was imposed that the bending moment and shear force were equal to zero at Γ_1. The results were compared with those obtained using the grdfft function of the Generic Mapping Tools (GMT; Wessel & Smith 1998, Fig. 5c). The GMT grdfft function takes the 2-D forward fast Fourier transform of the input data (load), calculates the isostatic response function in the frequency domain, convolves the transformed data with the isostatic response function and finally transforms back to the space domain.

It can be seen that in both cases (1-D load on a subducting plate and a 2-D load far away from a subduction zone) our method yields identical results than those produced by other tested and established methods.

3.2 Application to natural study cases along the Chilean margin

3.2.1 Juan Fernández seamounts

On the Nazca Plate, off Valparaíso, lies the JFR, which is almost perpendicular (N78.4°E) to the trench (Fig. 2). This mountain range is ~900 km long and has 11 mountains (extinct volcanoes) which extend from the hot spot (97.5°W/34°S), west of the island Alexander Selkirk to the O'Higgins seamount (von Huene *et al.* 1997). The hypothesis that the JFR formed in the hotspot is held by the linear increase in age along the ridge as was inferred from magnetic data (Yáñez *et al.* 2001).

The JFR forms a barrier for trench turbidites transport coming from the south. The sedimentary fill of the trench between 34°S and 45°S varies between 1.5 and 2.5 km depth, while north of the ridge sediments reach only about 500 m thick (von Huene *et al.* 1997). Near the trench there are two prominent volcanic domes, located ~70 km west of the trench in front of Valparaíso city: the O'Higgins Guyot and the O'Higgins seamount. Their base are located about 4 km deep under the sea level and rise above the ocean floor to a height of 3.5 km in the case of O'Higgins Guyot and 2.9 km the O'Higgins seamount. The difference in size is best appreciated when we compare their respective volumes: the O'Higgins Guyot (base diameter of ~27 km) has a volume of 668 $\mathrm{km^3}$ ± 10 per cent, while O'Higgins seamount (base diameter of ~15 km) has a volume estimated at 177 $\mathrm{km^3}$ ± 10 per cent above the ocean floor (Kopp *et al.* 2004).

The O'Higgins seamount formed about 9 Ma which has been inferred from its magnetic signal (Yáñez *et al.* 2001). To the east of the trench there is a prominent magnetic anomaly located at 72.6°W/32.7°S which would indicate the location of the Papudo seamount which already subducted under the continental plate (Yáñez *et al.* 2001).

Within this context we calculated the flexure under the O'Higgins Guyot and the O'Higgins seamount, for which we used a mesh as the one shown in Fig. 3(c). The area closest to the trench (S1) ranges from 0 to 60 km away from the trench, the second area (S2) from 60 to 150 km and the third from 150 km to the end of the plate (S3).

The boundary conditions used for the Juan Fernández seamounts domain (Fig. 3c) were

$$
\begin{aligned}
\Gamma_1 &: \quad \vec{M} = -\vec{M}_0 = -M_0\hat{\beta}, \quad V = -V_0 \\
\Gamma_2 &: \quad \vec{M} = 0, \quad V = 0 \\
\Gamma_3 &: \quad w = 0, \quad \vec{\theta} = 0 \\
\Gamma_4 &: \quad \vec{M} = 0, \quad V = 0,
\end{aligned}
$$

where $\hat{\beta}$ corresponds to the unitary vector in the plate convergence direction (Fig. 4b).

A Monte Carlo method was used in order to find those values that minimize the difference between the calculated Moho and a gravimetric or reference one. For obtaining the latter, we constructed a velocity model and calculated its gravimetric effect, which was compared with the free-air gravity anomaly observed obtained from free global data sets (Sandwell & Smith 1997, Fig. 3b). The 2-D gravity calculation is based on Parker's spectral method (Parker 1973) (for details see Korenaga *et al.* 2001). The model is modified to minimize the misfit or rms error between observed and calculated gravity.

A mantle's density of 3300 $\mathrm{kg\,m^{-3}}$ was assumed. Initially a velocity model (V) was proposed (Sepúlveda 2012), as shown in Fig. 6, which then becomes a density model (ρ) using the following relations (Fig. 7):

Nafe & Drake (1963) relationship for the sedimentary section, $\rho = 1.75 + 0.16V$

Carlson & Herrick (1990) relationship for igneous upper crust, $\rho = 3.61'6.0/V$

Birch (1961) law for plagioclase, and diabase-gabbro ecoglite (lower crust), $\rho = 0.375(1 + V)$

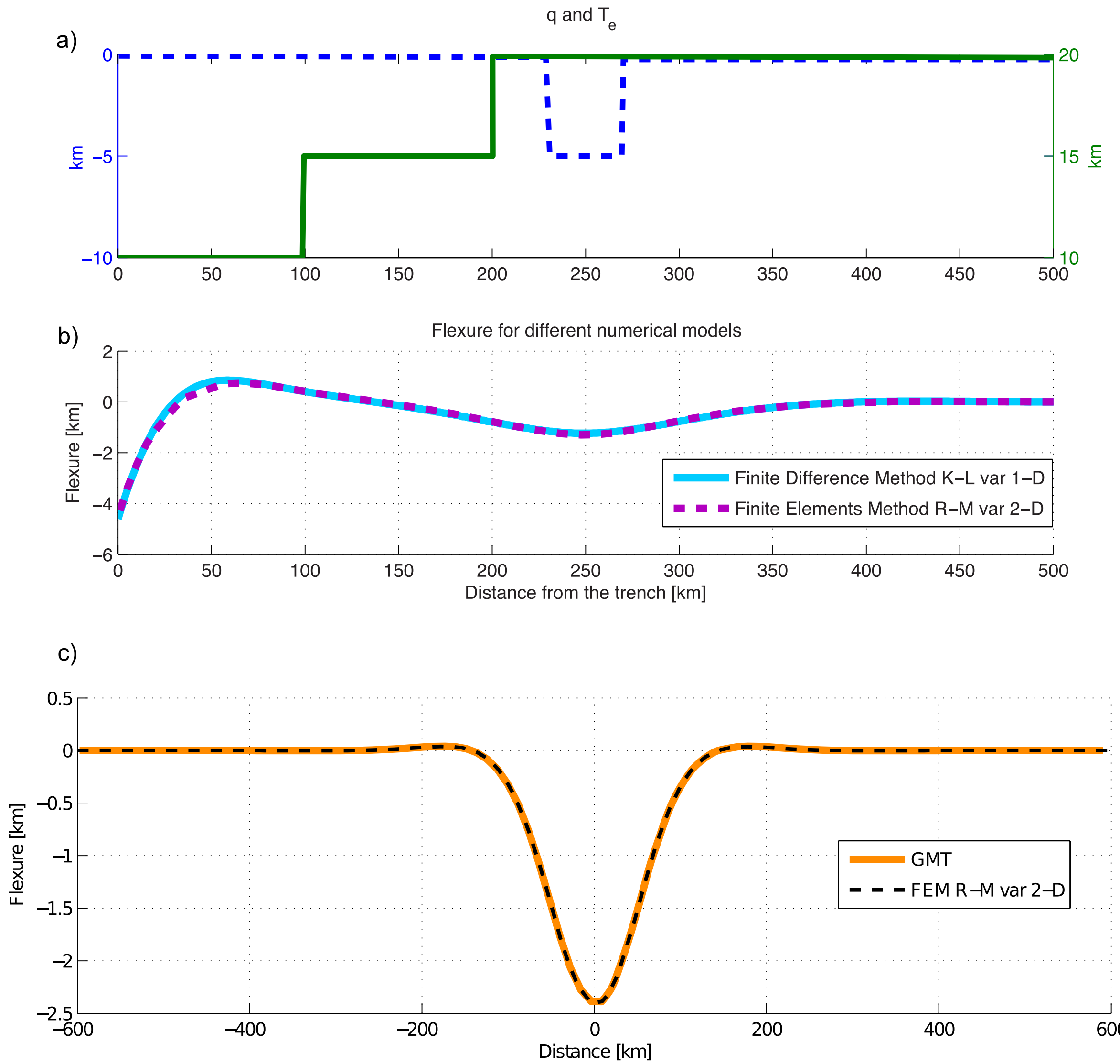

Figure 5. Comparison of model results with other methods. (a) A very long load in the perpendicular direction of the figure was applied over an elastic plate with variable elastic thickness. The load is shown in blue dashed line (left-hand axis) and the elastic thickness variation in green (right-hand axis). (b) Comparison of the flexure calculated using two different numerical models and methods near a subduction zone. In light blue we show the flexure calculated using the finite difference method used in Contreras-Reyes & Osses (2010) and in purple dashed line the Reissner–Mindlin model using the finite element method with $\beta = 0°$. For all calculations the same bending moment and boundary conditions were used. (c) Comparison of the flexure produced by a rectangular load of 100 km width, 100 km length and 5 km height calculated using a constant elastic thickness of 15 km far away from a subduction zone. In orange the GMT result and in black dashed line the result given by the finite element method for the Reissner–Mindlin thin plate model.

The rms error was calculated as follows:

$$\mathrm{rms} = \sqrt{\frac{1}{N}\sum_{i=0}^{N}\left(g_i^{\mathrm{obs}} - g_i^{\mathrm{calc}}\right)^2},$$

where N is the number of points along the profile, g^{obs} the observed gravity (data) and g^{calc} the gravity calculated using the proposed density model.

With the previous model we obtain the best Moho along the three studied profiles (P01, P02 and P03) shown in Fig. 3(a). The obtained Moho for profile P01 is then compared with our flexure calculations results.

For calculating the flexure for the Juan Fernández region, we performed another Monte Carlo approach, where the maximum outer-rise height w_b (Fig. 1) was varied between 0.2 and 0.7 km in steps of 0.1 km, its position x_b between 70 and 100 km in steps of 10 km, the elastic thickness in the sector S1 between 10 and 20 km, in sector S2 between 2 and 10 km and in S3 between 10 and 20 km in steps of 1 km. We chose a different range below the seamounts after performing some tests using our 3-D model and a 2-D model as the one shown in Contreras-Reyes & Osses (2010). We found that high elastic thickness were not able to adjust the observed Moho. The values of the Monte Carlo parameters determine the value of the bending moment and the shear force. The rest of the parameters used correspond to those shown in Table 1.

To quantify the associated error we calculated the rms error in metres as follows:

$$\mathrm{rms} = 1000\sqrt{\frac{1}{N}\sum_{i=0}^{N}\left(\mathrm{Moho}_i^{\mathrm{real}} - \mathrm{Moho}_i^{\mathrm{calc}}\right)^2},$$

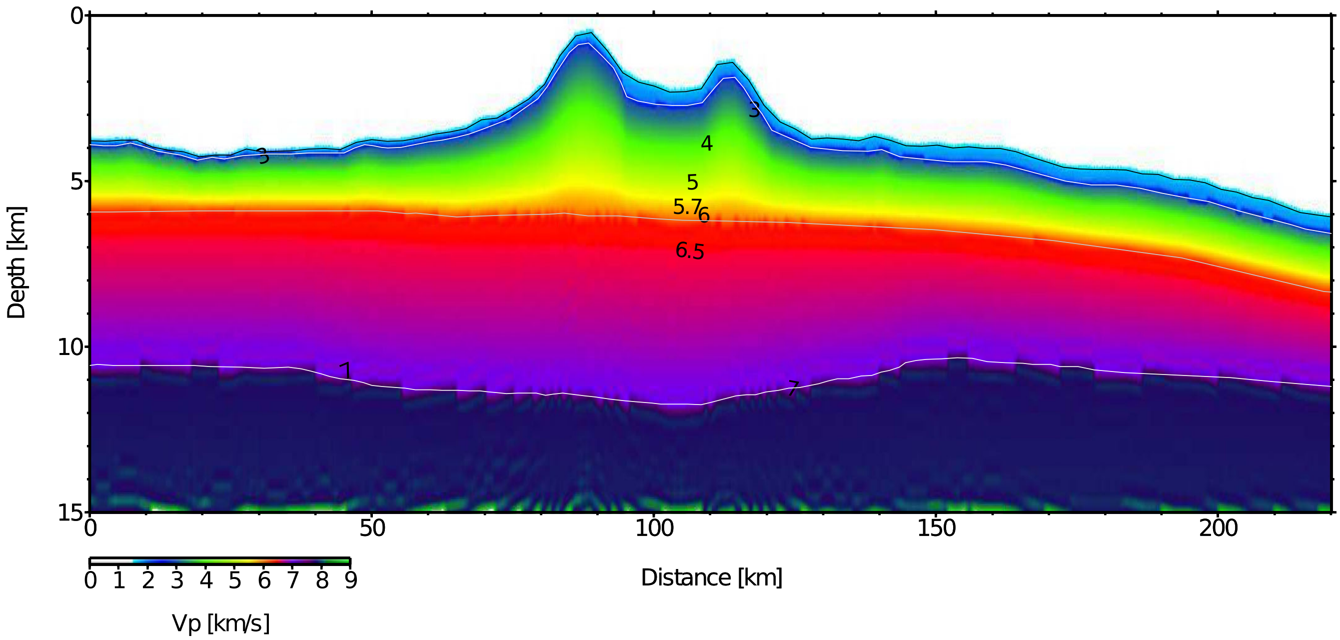

Figure 6. Proposed velocity model for profile P01. This will be used for calculating the gravity anomaly, which subsequently will be compared with the observed data. The proposed Moho is based on the work of Contreras-Reyes & Sepúlveda (2011).

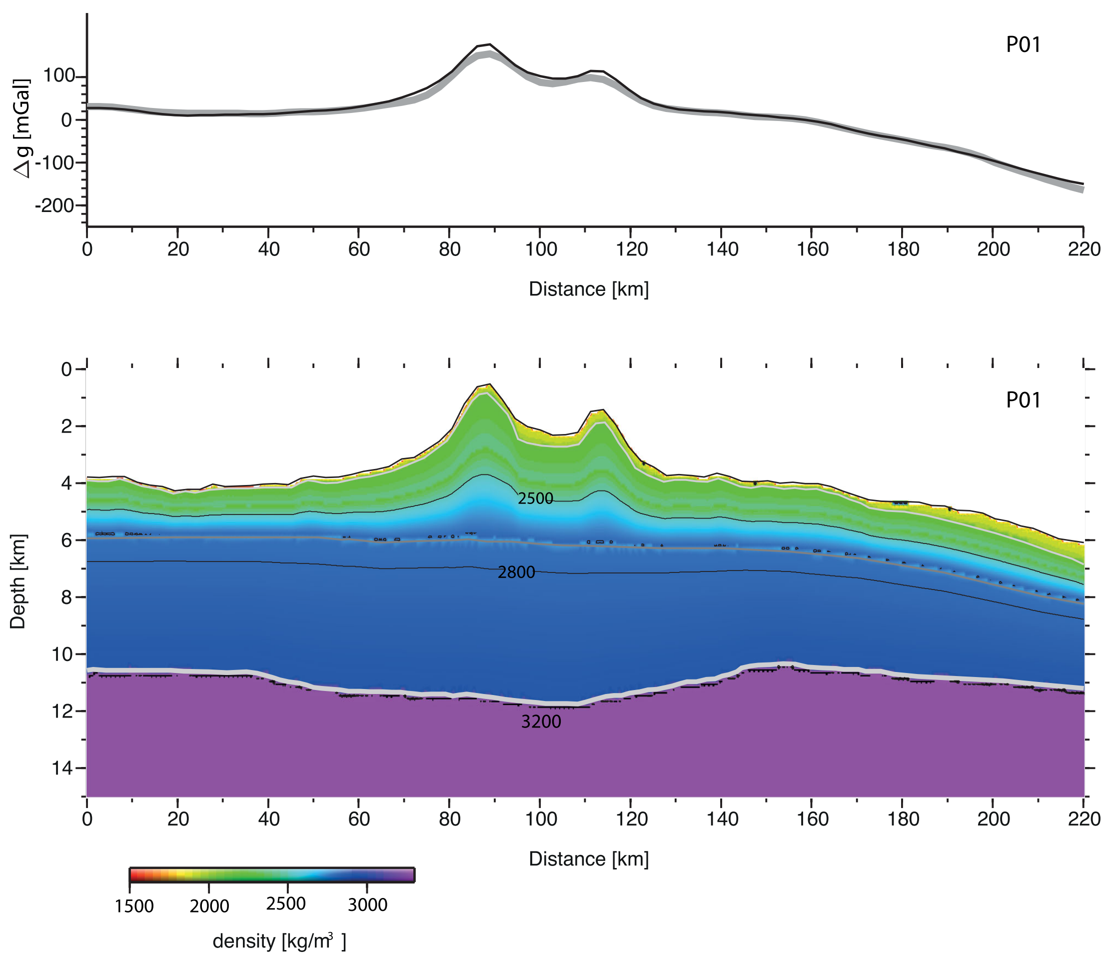

Figure 7. Top panel: in black line he observed Bouguer anomaly along the bathymetric profile P01 shown in Fig. 3(a), and Bouguer anomaly calculated from the density model shown below in grey line. The rms error is ∼7.6 (mGal). Bottom panel: density model for profile P01.

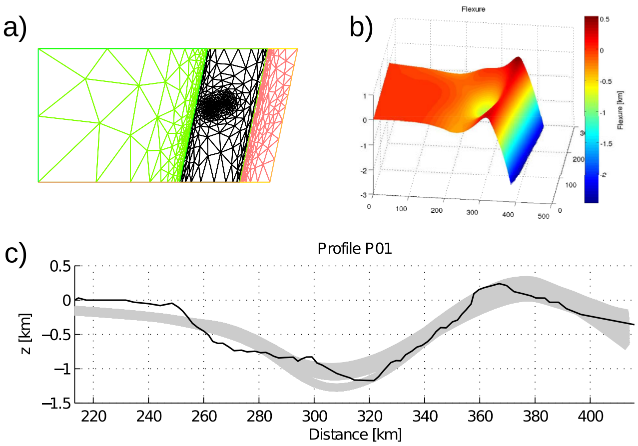

Figure 8. (a) Final mesh used for calculating the flexure using the FEM under the O'Higgins seamounts. The initial mesh (Fig. 3c) was refined under the seamounts for more precision under the most important features. (b) 3-D view of the flexure of the Moho under the seamounts using the R–M model with variable elastic thickness. (c) In grey the various possible solutions for profile P01, whose rms error did not exceed 150 m. In black the reference gravimetric Moho. The solutions were extracted from the different calculated surfaces as the one in Fig. 8(b). It can be seen that the fit is quite reasonable. The average value of elastic thickness for the area closest to the trench was ∼12.8 km, for the area just below the seamounts of ∼5 km and for the area farthest of ∼15.2 km.

where N is the number of points, $\mathrm{Moho}^{\mathrm{real}}$ the vertical coordinate (in km) of the reference gravimetric Moho and $\mathrm{Moho}^{\mathrm{calc}}$ the vertical coordinate of the calculated Moho using finite elements.

In this study region the Nazca Plate converges in a direction N78.4°E so it was decided to set the angle β at 11.6°. The mesh used for calculating the flexure was refined under the seamounts in order to achieve more precision under the most important features (Fig. 8a). As an example, Fig. 8(b) shows one of the resulting surfaces obtained. Once the surface is calculated we proceed to extract data for profile P01 to compare with the gravimetric Moho. The results in which rms error, in metres, was less than 150 m are shown in Fig. 8(c). The minimum value found for the elastic thickness in the S1 was 10 km, while the maximum was 18 km. For sector S2 the minimum T_e was 4 km and the maximum of 6 km. For S3, the further sector from the trench, the minimum was 10 km and the maximum of 20 km. The average values obtained for the elastic thickness, whose rms did not exceed 150 m were: $T_e^1 \approx 13$ km [standard deviation (SD) = 2.05 km], $T_e^2 \approx 5$ km (SD = 0.28 km) and $T_e^3 \approx 15$ km (SD = 3.03 km). The trend is that the elastic thickness reaches its minimum value just below the seamounts and its maximum value in the zone farthest from the trench. Results for the Juan Fernández region are summarized in Table 2.

Table 2. The table shows the elastic thickness results (in km) found for the Juan Fernanández region from the FEM flexural modelling. These results have an rms error that does not exceed 150 m.

Distance from the trench (km)	Minimum T_e	Maximum T_e	Average T_e	SD
0–60	10	18	13	2.05
60–150	4	6	5	0.28
150–end	10	20	15	3.03

3.2.2 *Arica Bend*

The second study area is part of what is known as the Arica Bend (Fig. 4a). This area is of great interest because the margin around 18°S changes its orientation from a NNE at the south to a NW to the north. This implies that the convergence direction goes from being almost perpendicular to the trench to an oblique direction. This feature requires a flexural model that can consider a 3-D geometry. Also in this area the age of the Nazca Plate increases from 30 Ma at the north to 45 Ma at the south along the trench.

Numerous palaeomagnetic studies indicate that the Arica Bend formed due to rotations of the plate (Prezzi & Vilas 1998; Kley 1999; Arriagada *et al.* 2008), however, there is no agreement on the magnitude of these because the estimates of crustal shortening produced by a turnover margin are not consistent with the observations. Other authors attribute the formation of the Arica Bend to the existence of a period of flat subduction between 37 and 25 Ma which generated compression and crustal shortening (O'Driscoll *et al.* 2012). The formation of flat subduction is attributed to a combined effect between the subduction of a buoyant piece of the Manihiki Plateau during the late Eocene and the suction effect due to the pressure generated by the flow of the mantle as the plate subducts under the Amazonian craton (O'Driscoll *et al.* 2012).

The unique geometry of the Arica Bend region is characterized by the variable convergence direction change, which makes the bending moment also vary. We chose a very large area to study the flexure caused only by the subduction process, and thus ignoring the small ridges on the plate. For the flexure calculation the domain was divided into four distinct regions (Fig. 9a) in order to vary the elastic thickness in each of them using a Monte Carlo method. The first region, the closest to the trench (red) has a width of 30 km approximately. The second region, coloured yellow, also has a width of about 30 km. The third region, shown in green, has a width of 60 km; and finally the fourth region is that shown in blue covering most of the plate.

The boundary conditions used for the domain shown in Fig. 4(a) were

$$\begin{aligned}
\Gamma_1 &: \quad \vec{M} = -\vec{M}_0 = -M_0\hat{\beta}, \quad V = -V_0 \\
\Gamma_2 &: \quad w = 0, \quad \vec{\theta} = 0 \\
\Gamma_3 &: \quad \vec{M} = 0, \quad V = 0.
\end{aligned}$$

In the Monte Carlo analysis we varied w_b from 0.1 to 1.5 km in steps of 0.1 km, x_b from 70 to 100 km in steps of 10 km and the

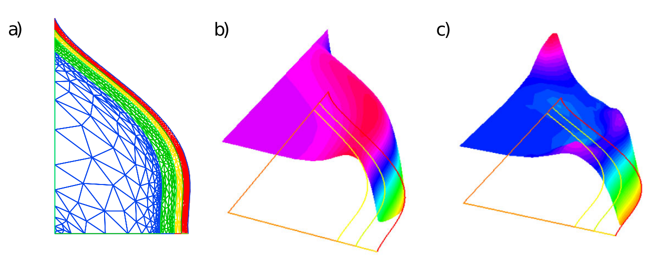

Figure 9. (a) Mesh used by the FEM for calculating the flexure for the Arica Bend region using the R–M model. The domain was divided into four distinct regions in which the elastic thickness was varied using a Monte Carlo method. The first region, the closest to the trench (red) has a thickness of 30 km approximately. The yellow region also has a thickness of about 30 km. The green region has a thickness of 60 km and finally the fourth region is the one shown in blue which covers most of the plate. (b) Example of flexure calculated using R–M model with variable elastic thickness through the FreeFem++ software. (c) Loaded filtered bathymetry of the Arica Bend used for calculating the rms error.

elastic thicknesses of each of the regions from 14 to 36 km in steps of 1 km and from 36 to 40 km in steps of 2 km. These values determine the value of the bending moment. The rest of the parameters used correspond to those shown in Table 1.

To calculate the rms error associated with the result, it was decided to filter the bathymetry, in order to remove defects that were not produced by the flexure. The rms error (in metres) was calculated as follows:

$$\mathrm{rms} = 1000\sqrt{\frac{\int(\mathrm{err})\mathrm{d}x\,\mathrm{d}y}{Area}},$$

where err corresponds to the square modulus of the difference between the calculated geometry in FreeFem++ (Fig. 9b) and the filtered bathymetry (Fig. 9c) and *Area* is the area considered in the study zone. Given the boundary conditions, especially the one that states that there is no deflection at border Γ_2, we decided to calculate the rms error in an area smaller than the total area of the zone, so we can neglect the error associated to that boundary, especially in the far north, where there are also bathymetric heights unrelated to the bending and that were not possible to filter completely. The smaller area considered covers well profiles P04, P05, P06 and P07 (Fig. 4a).

Finally, the best results were chosen, those whose rms error did not exceed 140 m and profiles P04, P05, P06 and P07 were extracted. Fig. 10 shows the 16 best results for each of the profiles in grey, the real bathymetry in black doted line and the filtered bathymetry in solid blue line. The red dashed line corresponds to the solution given by the finite differences method presented in Contreras-Reyes & Osses (2010) for a 1-D Kirchhoff–Love Plate model using the average values found for the best results shown in grey. The vertical lines show the divisions of the plate were elastic thickness was varied. In profile P06 it can be seen that the filter could not effectively remove the large bathymetric high.

The minimum value among the 16 best fits of the elastic thickness of the first region (closest to the trench) was 20 km, the maximum of 28 km while the average was ~23 km with a *SD* of 2.7 km. For the second region (yellow in Fig. 9a) the minimum was 15 km, a maximum of 20 km and the average ~18 km with a *SD* of 1.4 km. For the third area (green in Fig. 9a) the minimum was 14 km, the maximum of 18 km and the average of ~16 km with a *SD* of 1.3 km. Finally, for the region furthest from the trench (blue in Fig. 9a) the minimum was 14 km, the maximum of 40 km and the average of ~25 km with a *SD* of 5 km, from which we can conclude that this method cannot determine the elastic thickness of the portion furthest from the trench, were very little flexure can be appreciated. The 3-D model represented by the grey curves show a better fit than the 1-D model (red dashed curve) in the region nearest to the trench. Results for the Arica Bend region are summarized in Table 3.

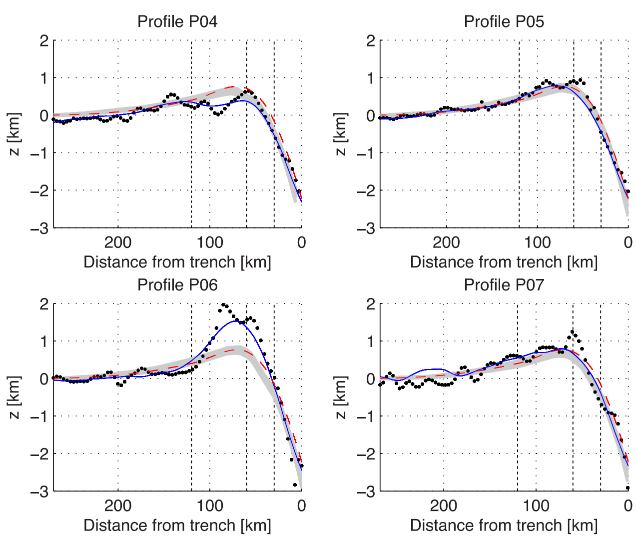

Figure 10. The dotted curve shows the real bathymetry for profiles P04, P05, P06 and P07 located at the Arica Bend region (Fig. 4). The blue curve shows the filtered bathymetry and the grey lines show the 16 best fit with an rms error less than 140 m. The red dashed curves shows the result given by the finite difference method for a 1-D Kirchhoff–Love model.

Table 3. The table shows the elastic thickness results (in km) found for the Arica Bend region from the FEM flexural modelling. These results have an rms error that does not exceed 140 m.

Distance from the trench (km)	Minimum T	Maximum T_e	Average T_e	*SD*
0–30	20	28	23	2.7
30–60	15	20	18	1.4
60–120	14	18	16	1.3
120–end	14	40	25	5

4 DISCUSSION AND CONCLUSIONS

4.1 Model scope

Although in nature all structures are 3-D, the exact analysis of the stresses and strains presents important difficulties. However, such precision is rarely necessary, and therefore justified, since usually the magnitude and distribution of the load, as well as strength and stiffness of the material studied, are not known with precision. There is an agreement that thin plate theory is a successful approach (Watts *et al.* 1975; Comer 1983; Wolf 1985; Braitenberg *et al.* 2002, among others).

The 2-D Kirchhoff–Love model corresponds to a simplification of the R–M model, and as discussed above, considers a fifth hypothesis that ultimately results in a dependence of the bending moment and the resulting deflection, only on the vertical deformations. Nevertheless, the most widely used models include one more simplification considering a 1-D model (Hanks 1971; McAdoo *et al.* 1978; Bodine *et al.* 1981; Judge & McNutt 1991; Bry & White 2007; Contreras-Reyes & Osses 2010), that is, a model in which the three-dimensionality of the problem is lost and can not work with localized loads or margins with complex geometries such as the Arica Bend.

The combination of plate bending and viscoelasticity (Morra & Regenauer-Lieb 2006) is out of our model's scope. The model presented in this paper is a simple model based on the thin shell approach using few simplifications, able to calculate the flexure of a plate produced by the combined effect of 3-D loads and bending associated with subduction. It also allows working with margins with complex geometries and variable elastic thickness along the plate which allows the identification of weaker areas of the lithosphere that can result from thermal alterations, brittle deformation or even rheological changes as discussed below.

4.2 Elastic thickness

The magnitude of the elastic thickness can be controlled by several physical mechanisms, some of them presented in the next subsections.

4.2.1 Plate age and thermal state

Previous work (e.g. Parsons & Molnar 1976) suggest that the estimates of oceanic lithosphere elastic thickness more or less follows the depth of the isotherm of 600 °C and that as the plate cools with time it becomes stronger and thus the elastic thickness increases (Caldwell *et al.* 1976). It is widely accepted that significant deviations of observed T_e from the predicted values are associated with thermal anomalies (McNutt & Menard 1982; Burov & Diament 1995), as might be the action of a hot spot. When a load is placed on a plate, it responds almost instantaneously (Bodine *et al.* 1981), so that the value of elastic thickness inferred for the area of Juan Fernandez would be a lower bound, that is, corresponds to the value of T_e at the time of the appearance of the seamount. This is because as time goes on, the plate gets older, cooler and becomes more rigid (Billen & Gurnis 2005).

This dependence of the elastic thickness on age has not been exempt of discussions and inconsistencies (Bry & White 2007). Using a simple plate cooling model (Caldwell & Turcotte 1979), we would expect that the elastic thickness for the area of Juan Fernández was about ∼20 km and for the Arica Bend area of about ∼40 km. The values found in this work for T_e are much lower than those predicted by a thermal model, which suggests that the age of the plate is not the main factor determining the elastic thickness.

4.2.2 Geometry

Margin geometry in the Arica Bend region makes the three-dimensionality of the problem to increase the maximum amplitude of outer rise ($w_b \sim 650$ m). The assumption of a unidimensional model would overestimate the value of flexural rigidity (Watts *et al.* 1975; Contreras-Reyes & Osses 2010).

4.2.3 Inelastic deformation and hydrofracturing

Purely elastic plate models considering a constant elastic thickness are self-inconsistent because they usually predict intra-plate stresses large enough [in some cases close to 500 MPa (McAdoo *et al.* 1978; Capitanio *et al.* 2009)] to produce inelastic deformation (brittle or ductile). That is why models that combine elastic with plastic deformation have been able to explain more satisfactorily the amplitude and wavelength of the outer rise (McAdoo *et al.* 1978), however tend to overestimate the elastic thickness (Bodine & Watts 1979).

The strategy followed in this work was to use an elastic model with a variable elastic thickness (as in the work of Judge & McNutt 1991; Contreras-Reyes & Osses 2010) because inelastic behaviour reduces the local resistance of the plate (Billen & Gurnis 2005) and as a result it deflects as if the effective elastic thickness had decreased in some areas (Bodine & Watts 1979; Bodine *et al.* 1981; Burov & Diament 1995).

Results obtained for the elastic thickness under the Juan Fernández seamounts are consistent because the interaction between the hot spot and the lithosphere may have weakened the plate, and because the fact that we find a greater curvature may indicate the plate may have undergone inelastic deformation which could justify a reduction of the elastic thickness.

At the top of the outer rise, extensional faults associated with the deflection of the plate were observed and evidenced by horst and graben structures (Ranero *et al.* 2005) and seismicity (Christensen & Ruff 1983). These extensional faults allow fluid percolation within the crust and upper mantle, which may result in serpentinization of the latter. Pore pressure increment and fractures are mechanisms that significantly reduce the rock's strength (Brace & Kohlstedt 1980).

Given the above, it seems reasonable to find a lower elastic thickness at the outer rise in both zones: Juan Fernández and the Arica Bend. Our results are in agreement with a previous spectral isostatic study were significant weakening of the oceanic Nazca Plate approaching the trench was inferred (Tassara *et al.* 2007). They further speculated that along-strike variation in the strength of subducting plate could be related to variations in the degree of hydration and serpentinization of the oceanic upper mantle.

4.2.4 Horizontal forces

In areas where there are active spreading centres or where there is compression, the strength of the lithosphere could be reduced by horizontal forces. For example, in most elastic models, including the one proposed in this paper, the tectonic horizontal force is ignored because various studies have shown that does not greatly affect the deflection of the elastic plate unless stresses reach higher values than 10 kbar (Caldwell *et al.* 1976). However, if a plate's behaviour is not purely elastic, the horizontal force can produce surface faulting and reduce the value of elastic thickness decreasing the flexural rigidity of the plate (Caldwell *et al.* 1976; Bodine *et al.* 1981; Burov & Diament 1995). Currently it is not possible to determine the values of the involved horizontal forces through bathymetry analysis so additional data would be required, such as focal mechanisms of earthquakes with hypocentres near the trench, as was proposed by Hanks (1971). Other authors have proposed that the value of the horizontal force can vary considerably depending on the model used (Bodine & Watts 1979), so that its determination is still debated. Note that horizontal forces are easily included in our model by adding a term $-F\nabla w$ in eq. (1), where F represents the horizontal force. This term does not modify boundary conditions (4).

4.3 Conclusions

The above results show that for the Juan Fernández area the elastic plate thickness decreases significantly under the seamounts, that is, in the area of greatest curvature. These results are consistent with previous work (Burov & Diament 1995; Bry & White 2007).

In the case of the Arica Bend area, the results show that the elastic thickness tends to decrease in the portion of the outer rise, which can be interpreted as a result of plate weakening due to bending, fluid percolation or rheological changes.

The results do not support a simple relationship between age and elastic thickness of the plate. The resistance of the plate to deformation is probably strongly dominated by the involved stresses, which could produce inelastic deformation and thus reduce the effective elastic thickness, by changes on the lithosphere thickness, by thermal anomalies or compositional changes.

Unlike this model, previous studies usually consider simple geometries and 1-D loading, so that the model presented in this paper is a more general model that allows to work with complex margins and 3-D loads. However, this method has two main limitations. The first one is related to the large number of parameters to be fitted, which may lead to the non uniqueness of the solutions. At this point, further geodynamic interpretation of the results should be made cautiously. The second important limitation is that it is not able to determine the elastic parameters for the plate portion that has undergone little or no deformation. Despite the fact that our model is not accurate it gives an improved possibility to model the flexure caused by complex 3-D loading and could be a starting point for future numerical innovations.

ACKNOWLEDGEMENTS

The authors thank the useful comments and suggestions from the Editor Stephane Labrosse and the two reviewers, Gabriele Morra and Andrés Tassara. PM was supported by FONDECYT grant No. 11090009 through a Masters scholarship. AO also acknowledges FONDECYT 1110290 and CONICYT ACT1106 grants.

REFERENCES

Angermann, D., Klotz, J. & Reigber, C., 1999. Space-geodetic estimation of the Nazca-South America Euler vector, *Earth planet. Sci. Lett.,* **171**(3), 329–334.

Arriagada, C., Roperch, P., Mpodozis, C. & Cobbold, P.R., 2008. Paleogene building of the Bolivian Orocline: Tectonic restoration of the central Andes in 2-D map view, *Tectonics,* **27**(6), TC6014, doi:10.1029/2008TC002269.

Billen, M.I. & Gurnis, M., 2005. Constraints on subducting plate strength within the Kermadec trench, *J. geophys. Res.,* **110**(B5), B05407, doi:10.1029/2004JB003308.

Birch, F., 1961. The velocity of compressional waves in rocks to 10 kilobars. Part 2, *J. geophys. Res.,* **66**(7), 2199–2224.

Bodine, J.H. & Watts, A.B., 1979. On lithospheric flexure seaward of the Bonin and Mariana trenches, *Earth planet. Sci. Lett.,* **43**(1), 132–148.

Bodine, J.H., Steckler, M.S. & Watts, A.B., 1981. Observations of flexure and the rheology of the oceanic lithosphere, *J. geophys. Res.,* **86**(B5), 3695–3707.

Brace, W.F. & Kohlstedt, D.L., 1980. Limits on lithospheric stress imposed by laboratory experiments, *J. geophys. Res.,* **85**(B11), 6248–6252.

Braess, D., 2007. *Finite Elements: Theory, Fast Solvers, and Applications in Elasticity Theory,* 3rd edn, Cambridge Univ. Press.

Braitenberg, C., Ebbing, J. & Gotze, H., 2002. Inverse modelling of elastic thickness by convolution method—the eastern Alps as a case example, *Earth planet. Sci. Lett.,* **202**(2), 387–404.

Bry, M. & White, N., 2007. Reappraising elastic thickness variation at oceanic trenches, *J. geophys. Res.,* **112**(B08414), doi:10.1029/2005JB004190.

Burov, E.B. & Diament, M., 1995. The effective elastic thickness (Te) of continental lithosphere: what does it really mean? *J. geophys. Res.,* **100**(B3), 3905–3927.

Caldwell, J.G. & Turcotte, D.L., 1979. Dependence of the thickness of the elastic oceanic lithosphere on age, *J. geophys. Res.,* **84**(B13), 7572–7576.

Caldwell, J.G., Haxby, W.F., Karig, D.E. & Turcotte, D.L., 1976. On the applicability of a universal elastic trench profile, *Earth planet. Sci. Lett.,* **31**(2), 239–246.

Capitanio, F.A., Morra, G. & Goes, S., 2009. Dynamics of plate bending at the trench and slab-plate coupling, *Geochem. Geophys. Geosyst.,* **10**(4), Q04002, doi:10.1029/2008GC002348.

Carlson, R.L. & Herrick, C.N., 1990. Densities and porosities in the oceanic crust and their variations with depth and age, *J. geophys. Res.,* **95**(B6), 9153–9170.

Christensen, D.H. & Ruff, L.J., 1983. Outer-rise earthquakes and seismic coupling, *Geophys. Res. Lett.,* **10**(8), 697–700.

Comer, R.P., 1983. Thick plate flexure, *Geophys. J. R. astr. Soc.,* **72**(1), 101–113.

Contreras-Reyes, E. & Osses, A., 2010. Lithospheric flexure modelling seaward of the Chile trench: implications for oceanic plate weakening in the Trench Outer Rise region, *Geophys. J. Int.,* **182**(1), 97–112.

Contreras-Reyes, E. & Sepúlveda, J., 2011. Magmatic processes beneath the Louisville and Juan Fernández hotspot tracks from wide angle seismic data. Poster at the American Geophysical Union Chapman Conference, Puerto Ayora, Galápagos, Ecuador.

Hanks, T.C., 1971. The Kuril Trench - Hokkaido rise system: large shallow earthquakes and simple models of deformation, *Geophys. J. R. astr. Soc.,* **23**(2), 173–189.

Harris, R.N. & Chapman, D.S., 1994. A comparison of mechanical thickness estimates from trough and seamount loading in the southeastern Gulf of Alaska, *J. geophys. Res.,* **99**(B5), 9297–9317.

Hertz, H., 1884. On the equilibrium of floating elastic plates, *Wiedemann's Annalen,* **22,** 449–455.

Hull, A.J., 2004. An exact analytical expression of the shear coefficient in the Mindlin plate equation. *Technical report, Naval Undersea Warfare Center Division,* Newport, Rhode Island.

Judge, A. & McNutt, M., 1991. The relationship between plate curvature and elastic plate thickness: a study of the Peru-Chile trench, *J. geophys. Res.,* **96**(B10), 16 625–16 639.

Kley, J., 1999. Geologic and geometric constraints on a kinematic model of the Bolivian Orocline, *J. South Am. Earth Sci.,* **12**(2), 221–235.

Kopp, H., Flueh, E.R., Papenberg, C. & Klaeschen, D., 2004. Seismic investigations of the O'Higgins seamount group and Juan Fernández Ridge: aseismic ridge emplacement and lithosphere hydration, *Tectonics,* **23**(2), doi:0.1029/2003TC001590.

Korenaga, Jun, Holbrook, W.S., Detrick, R.S. & Kelemen, P.B., 2001. Gravity anomalies and crustal structure at the southeast Greenland margin, *J. geophys. Res.,* **106**(B5), 8853–8870.

Levitt, D.A. & Sandwell, D.T., 1995. Lithospheric bending at subduction zones based on depth soundings and satellite gravity, *J. geophys. Res.,* **100**(B1), 379–400.

McAdoo, D.C., Caldwell, J.G. & Turcotte, D.L., 1978. On the elastic-perfectly plastic bending of the lithosphere under generalized loading with application to the Kuril Trench, *Geophys. J. R. astr. Soc.,* **54**(1), 11–26.

McNutt, M.K. & Menard, H.V., 1982. Constraints on yield strength in the oceanic lithosphere derived from observations of flexure, *Geophys. J. R. astr. Soc.,* **71,** 363–394.

Mindlin, R.D., 1951. Influence of rotatory inertia and shear on flexural motions of isotropic, elastic plates, *ASME J. Appl. Mech.,* **18,** 31–38.

Morra, G. & Regenauer-Lieb, K., 2006. A coupled solid-fluid method for modelling subduction, *Phil. Mag.,* **86**(21–22), 3307–3323.

Nafe, J.E. & Drake, C.L., 1963. Physical properties of marine sediments, in *The Sea: Ideas and Observations on Progress in the Study of the Seas,* Vol. 3, pp. 794–815. Interscience Publishers.

O'Driscoll, L., Richards, M. & Humphreys, E., 2012. Nazca-South America interactions and the late Eocene-late Oligocene flat-slab episode in the central Andes, *Tectonics,* **31**(2), TC2013, doi:10.1029/2011TC003036.

Parker, R.L., 1973. The rapid calculation of potential anomalies, *Geophys. J. R. astr. Soc.,* **31**(4), 447–455.

Parsons, B. & Molnar, P., 1976. The origin of outer topographic rises associated with trenches, *Geophys. J. R. astr. Soc.,* **1**(4), 707–712.

Prezzi, C. & Vilas, J., 1998. New evidence of clockwise vertical axis rotations south of the Arica elbow (Argentine Puna), *Tectonophysics,* **292**(1–2), 85–100.

Ranero, C.R., Villaseñor, A., Phipps Morgan, J. & Weinrebe, W., 2005. Relationship between bend-faulting at trenches and intermediate-depth seismicity, *Geochem. Geophys. Geosyst.,* **6**(12), Q12002, doi:10.1029/2005GC000997.

Reissner, E., 1945. The effect of transverse shear deformation on the bending of elastic plates, *ASME J. Appl. Mech.,* **12,** A68–A77.

Sandwell, D. & Smith, W., 1997. Marine gravity anomaly from Geosat and ERS 1 satellite altimetry, *J. geophys. Res.,* **102**(B5), 10 039–10 054.

Sepúlveda, J., 2012. Tomografía sísmica 2D de alta resolución bajo los montes submarinos O'Higgins. *Master's thesis,* Universidad de Chile. Available at: http://www.tesis.uchile.cl/handle/2250/112345 (last accessed September 2012).

Tassara, A., Swain, C., Hackney, R. & Kirby, J., 2007. Elastic thickness structure of South America estimated using wavelets and satellite-derived gravity data, *Earth planet. Sci. Lett.,* **253**(1–2), 17–36.

Turcotte, D.L. & Schubert, G., 2002. *Geodynamics*. Cambridge Univ. Press.

von Huene, R., Corvalán, J., Flueh, E.R., Hinz, K., Korstgard, J., Ranero, C.R. & Weinrebe, W. & the CONDOR Scientists, 1997. Tectonic control

of the subducting Juan Fernández Ridge on the Andean margin near Valparaiso, Chile, *Tectonics,* **16**(3), 474–488.
Walcott, R.I., 1970. Flexure of the lithosphere at Hawaii, *Tectonophysics,* **9**(5), 435–446.
Watts, A.B., 2001. *Isostasy and Flexure of the Lithosphere*. Cambridge Univ. Press.
Watts, A.B. & Talwani, M., 1974. Gravity anomalies seaward of deep-sea trenches and their tectonic implications, *Geophys. J. R. astr. Soc.,* **36**(1), 57–90.
Watts, A.B., Cochran, J.R. & Selzer, G., 1975. Gravity anomalies and flexure of the lithosphere: three-dimensional study of the great meteor seamount, Northeast Atlantic, *J. geophys. Res.,* **80**(11), 1391–1398.
Wessel, P., 1996. Analytical solutions for 3-D flexural deformation of semi-infinite elastic plates, *Geophys. J. Int.,* **124**(3), 907–918.
Wessel, P. & Smith, W., 1998. New, improved version of generic mapping tools released, *EOS, Trans. Am. geophys. Un.,* **79**(47), 579.
Wolf, D., 1985. Thick-plate flexure re-examined, *Geophys. J. R. astr. Soc.,* **80**(1), 265–273.
Yáñez, G., Ranero, C., von Huene, R. & Díaz, J., 2001. Magnetic anomaly interpretation across the southern central Andes (32°–34° S): the role of the Juan Fernández Ridge in the late Tertiary evolution of the margin, *J. geophys. Res.,* **106**(B4), 6325–6345.

APPENDIX A

A1 The Kirchhoff–Love plate model

It can be easily seen that if we add a fifth hypothesis, known as the 'normal hypothesis' or 'Kirchhoff's hypothesis', we can derive the Kirchhoff–Love equation of motion for an elastic plate. The fifth hypothesis says:

H5. *Normal hypothesis*. The deformations of normal vectors to the middle surface are again orthogonal to the (deformed) middle surface.

The normal hypothesis implies that the rotations are no longer independent of the deflections:

$$\left.\begin{aligned} \theta_i(x,y) &= \tfrac{\partial}{\partial x_i} w(x,y),\\ u_i(x,y,z) &= -z\tfrac{\partial w}{\partial x_i}(x,y), \end{aligned}\right\} \quad i = 1,2. \tag{A1}$$

If we take –div(1)+(2) we will get

$$\mathrm{div}\left[\mathrm{div}\left(T_e^3\sigma(\vec\theta)\right)\right] = g.$$

Now we apply the condition imposed by H5 given in (A1) obtaining

$$T_e^3\sigma(\vec\theta) = D\begin{bmatrix} \partial_{xx}w + \nu\partial_{yy}w & (1-\nu)\partial_{xy}w \\ (1-\nu)\partial_{xy}w & \nu\partial_{xx}w + \partial_{yy}w \end{bmatrix}.$$

Using that the divergence of a second order tensor corresponds to a vector which components are given by $\mathrm{div}(A_{ij}) = V_j = \sum_i \partial_i A_{ij}$ we will get the flexure differential equation for a variable elastic thickness under the Kirchhoff-Love model:

$$\partial_{xx}\left[D(\partial_{xx}w + \nu\partial_{yy})\right] + 2\partial_{xy}\left[D(1-\nu)\partial_{xy}w\right] + \partial_{yy}\left[D(\nu\partial_{xx}w + \partial_{yy})\right] = g. \tag{A2}$$

If additionally we suppose that the elastic thickness remains constant along the plate, and therefore the flexural rigidity also remains constant, the previous equation simplifies to:

$$D\nabla^4 w = g.$$

By replacing the value of the net vertical force we finally arrive to the well known flexure equation

$$D\nabla^4 w + (\rho_m - \rho_w)gw = q. \tag{A3}$$

A2 Variational formulation for the R–M plate model

We started from the R–M equations given in (1) and (2). We will multiply (1) by $\vec\psi$ (which we suppose zero on the same boundary where θ is zero) and integrate by parts over the whole domain Ω we obtain:

$$\int_\Omega T_e^3\sigma(\vec\theta) : \varepsilon(\vec\psi) - \int_{\partial\Omega} T_e^3\sigma(\vec\theta)\hat n\cdot\vec\psi - \int_\Omega \lambda^* T_e(\nabla w - \vec\theta)\cdot\vec\psi = 0,$$

where $A : B = \sum_{i,j} a_{ij}b_{ij}$ stands for the tensor product between matrices. If we impose the boundary conditions of Section 2.3, we obtain

$$\int_\Omega T_e^3\bar D(1-\nu)\varepsilon(\vec\theta) : \varepsilon(\vec\psi) + \int_\Omega T_e^3\bar D\nu\,\mathrm{div}(\vec\theta)\mathrm{div}(\vec\psi) - \int_\Omega \lambda^* T_e(\nabla w - \vec\theta)\cdot\vec\psi + \int_{\Gamma_1} M_0\hat\beta\cdot\vec\psi = 0. \tag{A4}$$

Now we multiply (2) by v (which we suppose zero on the same boundary where w is zero) and integrate by parts over Ω, then

$$\int_\Omega \lambda^* T_e(\nabla w - \vec\theta)\cdot\nabla v - \int_{\partial\Omega}\lambda^* T_e(\nabla w - \vec\theta)\cdot\hat n v + \int_\Omega \Delta\rho g\, w\, v = \int_\Omega q v$$

then, using the boundary conditions of Section 2.3 we obtain

$$\int_\Omega \lambda^* T_e(\nabla w - \vec\theta)\cdot\nabla v + \int_\Omega \Delta\rho g\, w\, v - \int_\Omega q v + \int_{\Gamma_1} V_0 v = 0. \tag{A5}$$

The variational formulation shown above corresponds to a problem that is badly conditioned, which can lead to shear locking (Braess 2007), in order to avoid this, it is suggested a mixed problem by introducing the normed shear term:

$$\vec\gamma := T_e\,\lambda^*(\nabla w - \vec\theta).$$

If we multiply by a test function $\vec\eta$ and integrate in Ω we will have a third integral that will conform our system:

$$\int_\Omega T_e\lambda^*(\nabla w - \vec\theta)\cdot\vec\eta - \int_\Omega \vec\gamma\cdot\vec\eta = 0. \tag{A6}$$

Finally, we add a fourth equation which will let us compute the bending moment easier:

$$d := \mathrm{div}(\vec\theta).$$

If we multiply by the test function e and by $T_e^3\bar D\nu$ and integrate in Ω we will get

$$\int_\Omega T_e^3\bar D\nu\,\mathrm{div}(\vec\theta)e - \int_\Omega T_e^3\bar D\nu\, d\, e = 0. \tag{A7}$$

The sum of eqs (A4)–(A7) makes the variational formulation. In summary, the variational formulation is the following:

Find $(\vec{\theta}, w, \vec{\gamma}, d)$ such that
$$\int_\Omega T_e^3 \bar{D}(1-\nu)\varepsilon(\vec{\theta}) : \varepsilon(\vec{\psi})$$
$$+ \int_\Omega T_e^3 \bar{D}\nu \operatorname{div}(\vec{\theta}) \operatorname{div}(\vec{\psi}) + \int_\Omega \vec{\gamma} \cdot (\nabla v - \vec{\psi})$$
$$+ \int_\Omega T_e \lambda^* (\nabla w - \vec{\theta}) \cdot \vec{\eta} - \int_\Omega \vec{\gamma} \cdot \vec{\eta} + \int_\Omega T_e^3 \bar{D}\nu \operatorname{div}(\vec{\theta}) e$$
$$- \int_\Omega T_e^3 \bar{D}\nu\, d\, e + \int_\Omega \Delta\rho g\, w\, v$$
$$= \int_\Omega q v - \int_{\Gamma_1} V_0 v - \int_{\Gamma_1} M_0 \hat{\beta} \cdot \vec{\psi} \quad \text{for all } (\vec{\psi}, v, \vec{\eta}, e),$$

where $(\vec{\theta}, w)$ and $(\vec{\psi}, v)$ are prescribed to be zero on the same boundaries, as indicated in Section 2.3. Notice that the term $\hat{\beta} \cdot \vec{\psi}$ should be written in an intrinsic reference system to the boundary, if $\hat{\beta} = (\cos\beta, \sin\beta)$ and $\hat{n} = (n_x, n_y)$ and $\tau = (-n_y, n_x)$ (see Fig. 9), then

$$\hat{\beta} \cdot \vec{\psi} = \begin{bmatrix} (n_x \cos\beta + n_y \sin\beta)(n_x \psi_1 + n_y \psi_2) \\ (n_x \sin\beta - n_y \cos\beta)(n_x \psi_2 - n_y \psi_1) \end{bmatrix}, \quad \text{(A8)}$$

where β is the subduction angle with respect to the horizontal reference.

SUPPORTING INFORMATION

Additional Supporting Information may be found in the online version of this article:

Figure 11. (top) Observed Bouguer anomaly along the bathymetric profile P02 shown in Fig. 2(b) in black line, and Bouguer anomaly, in grey line, calculated from the density model shown below. The rms error is ∼5.9 (mGal). (bottom) Density model for profile P02.

Figure 12. Top panel: Observed Bouguer anomaly along the bathymetric profile P03 shown in Fig. 2(b) in black line, and Bouguer anomaly, in grey line, calculated from the density model shown below. The rms error is ∼5 (mGal). Bottom panel: density model for profile P03.

(http://gji.oxfordjournals.org/lookup/suppl/doi:10.1093/gji/ggt464/-/DC1)

Please note: Oxford University Press is not responsible for the content or functionality of any supporting materials supplied by the authors. Any queries (other than missing material) should be directed to the corresponding author for the article.